Inorganic Chemistry
Cite This: Inorg. Chem. XXXX, XXX, XXX–XXX
Article
pubs.acs.org/IC

Effect of Thermally Induced Oxygen Vacancy of α-MnO_2 Nanorods toward Oxygen Reduction Reaction

X. Shi,[†,‡] H. Zheng,[*,‡] A. M. Kannan,[†] K. Pérez-Salcedo,[§] and B. Escobar[§]

[†]Fuel Cell Laboratory, The Polytechnic School, Ira A. Fulton Schools of Engineering, Arizona State University, Mesa, Arizona 85212, United States

[‡]Energy Centre, Council for Scientific and Industrial Research (CSIR), Pretoria, Gauteng 0184, South Africa

[§]Centro de Investigación Científica de Yucatán, Carretera Sierra Papacal − Chuburná Puerto, km 5. Sierra Papacal, Mérida, C.P. 97302, Yucatán, México

Supporting Information

ABSTRACT: MnO_2 has been explored for various applications in environmental and energy aspects. However, the thermal sensitivity of the MnO_2 crystal structure never been studied. As a potential cathode material for fuel cell, α-MnO_2 has a higher specific activity than Pt/C based on per metals cost. In this work, the physical and electrochemical properties of α-MnO_2 nanorods were explored for the first time under thermal treatment with different temperatures (300, 400, and 500 °C). Under thermal treatment, oxygen vacancies were induced. The high-angle annular dark-field (HAADF) images and electron energy loss spectroscopy (EELS) have been taken to explore oxygen vacancies of α-MnO_2 materials. From EELS and X-ray photoelectron spectroscopy (XPS) analysis, the oxygen vacancies on the α-MnO_2 nanorods were strengthened with the temperature increasing. The sample with 400 °C treatment exhibited the best performance toward ORR, excellent methanol tolerance and higher stability compared to commercial Pt/C in alkaline media due to its combination of preferable growth on (211) plane and moderate oxygen vacancies as well as coexistence of Mn (IV)/ Mn (III) species. It was also observed the α-MnO_2 nanorods tended to become longer and thinner with increasing temperature. This work suggests that the α-MnO_2 nanorods are thermal sensitive materials and their performance for ORR can be boosted under certain temperatures.

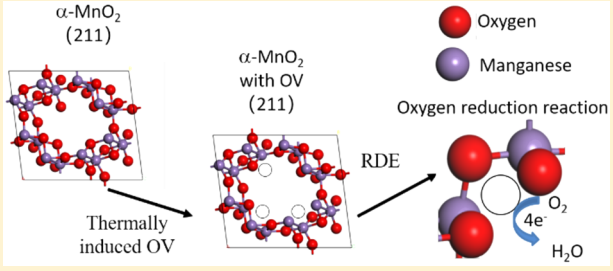

INTRODUCTION

The oxygen reduction reaction (ORR) has been widely studied and reported in recent decades,[1−3] due to its important role in energy conversion technologies, such as alkaline membrane fuel cell (AMFC),[4] microbial fuel cell,[5,6] direct methanol fuel cell (DMFC),[7] and energy storage (Li−air[2,3,8] and Zn−air[9−11] batteries). However, the low kinetic exchange current of ORR has slowed down the development and commercialization of those environmentally friendly technologies. Pt group metal (PGM) based catalysts deliver the highest ORR kinetic exchange current, but high cost, poor long-term durability, and easy poisoning are still big challenges to face. In particular, in DMFC, the Nafion membrane has a high methanol crossover rate; when methanol reaches the cathode, the ORR will be influenced by methanol oxidation.[7] Another approach is to develop non-PGM ORR catalysts. Among noble metal free ORR catalysts, manganese dioxides have received extensive attention due to the abundance of magnesium (10th element in the earth crust[12]) and the low cost, nonpoisonous nature, no impact on environment, and high stability. Additionally, manganese dioxides have many polymorphs (e.g., α-MnO_2, β-MnO_2, δ-MnO_2, γ-MnO_2, and λ-MnO_2) in which the basic building blocks, [MnO_6] octahedron, are assembled to different tunnel and layer structures.[13] Various crystal polymorphs lead to different electronic structures, which influence the electrochemical performance. Lu and co-workers reported Pt nanoparticle support on carbon and MnO_2 in acidic media and showed same activity and better durability compared to that of commercial Pt/C.[14] Li et.al studied MnO_2 N-doped carbon hybrid shell,[15] Hang et al. reported MnO_2-supported g-C_3N_4,[16] Zhang and co-workers studied phosphate-promoted α-MnO_2 in alkaline media toward ORR.[17] The published ORR data have been compared, and it was concluded that the specific current per dollar of α-MnO_2 is much higher than that of Pt/C due to the metal cost and high α-MnO_2 electrochemical properties.[18] In particular, α-MnO_2 shows onset potential and limiting current values close to those of the Pt/C benchmark in alkaline media toward ORR.

The ORR process can have a two or four electron transfer path, depending on the active sites of the catalytic surface. The two electron path can give a higher cell potential; however, the generated peroxides will bring damage to the membrane.[19] Typically, it is favorable to synthesis peroxides.[20] For fuel cell and metal air batteries, a four electron transfer path is desired.[21,22] The noble metal Pt mainly goes through directly

Received: February 19, 2019

DOI: 10.1021/acs.inorgchem.9b00492
Inorg. Chem. XXXX, XXX, XXX–XXX

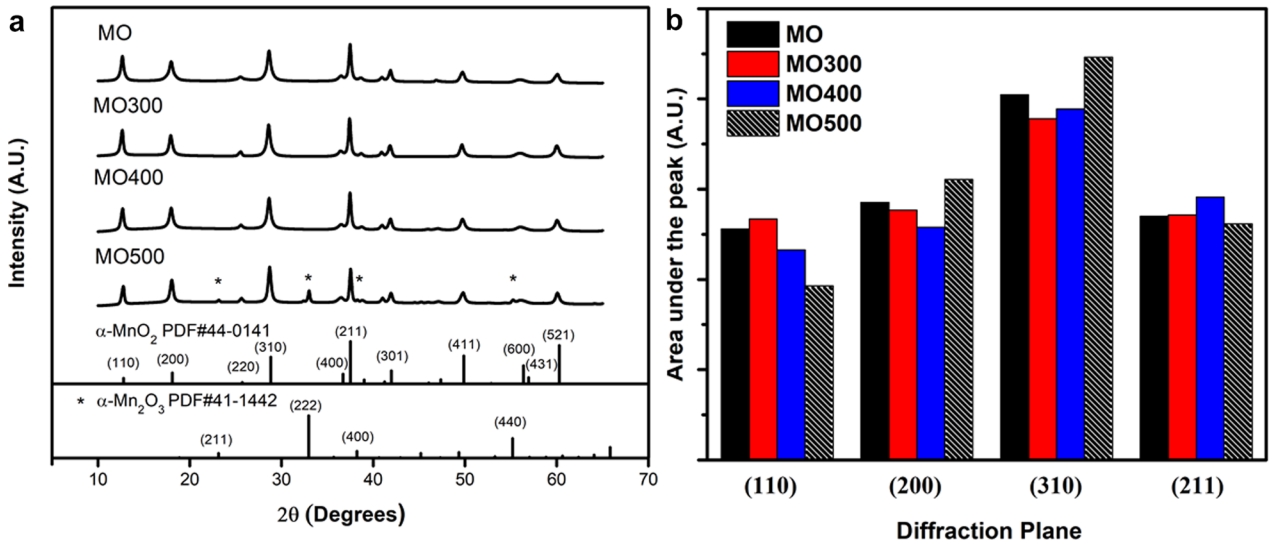

Figure 1. (a) X-ray diffractograms of MO, MO300, MO400, and MO500 samples. (b) Integrated diffraction intensity of each plane for all the samples.

four electron transfer, reducing the O_2 into OH^- in alkaline media (eq 1).[23−25] The ORR mechanism for α-MnO_2 has not yet been understood clearly; the commonly accepted mechanism was summarized in Cheng's paper.[26] First, oxygen molecule undergoes a two-electron partial reduction, forming HO_2^- (eq 2) and then further reducing into OH^- (eq 3) or decomposing into OH^- and O_2 (eq 4).[27,28] It has been reported that the catalytic speed of HO_2^- reduction or decomposition is infinitely fast compared to that ineq 2, so the generated peroxide ions will be reduced or decomposed immediately on the MnO_2 surface.[29−35] The MnO_2 reacts with water forming the active sites $Mn^{III}OOH$ (eq 5). The oxygen molecule either adsorbed onto two (eq 6a) or one generated $Mn^{III}OH$ (eq 6b) and then further reduced into OH^- (eq 7a) or HO_2^- (eq 7b), respectively. The route shown in eqs 5, 6a, and 7a illustrated eq 1 for the four electron transfer process, and the route shown in eqs 5, 6b, and 7b depicted eq 2 for the first two electron transfer reaction. Cheng's results showed that both routes exist in the ORR process in alkaline media.[26] Cao and co-workers have proposed that the increase in the concentration (above 3 M) will decrease the ORR performance, and the whole process rate should be controlled by the oxidizing of $Mn^{III}OOH$.[36]

$$O_2 + 2H_2O + 4e^- \rightarrow 4OH^- \quad (1)$$

$$O_2 + H_2O + 2e^- \rightarrow HO_2^- + OH^- \quad (2)$$

$$HO_2^- + H_2O + 2e^- \rightarrow 3OH^- \quad (3)$$

$$2HO_2^- \rightarrow 2OH^- + O_2 \quad (4)$$

$$MnO_2 + H_2O + e^- \leftarrow\rightarrow Mn^{III}OOH + OH^- \quad (5)$$

$$2Mn^{III}OOH + O_2 \leftarrow\rightarrow 2(Mn^{III}OOH\cdots O) \quad (6a)$$

$$Mn^{III}OOH + O_2 \leftarrow\rightarrow Mn^{III}OOH\cdots O_2 \quad (6b)$$

$$Mn^{III}OOH\cdots O) + e^- \leftarrow\rightarrow Mn^{IV}O_2 + OH^- \quad (7a)$$

$$Mn^{III}OOH\cdots O_2 + e^- \leftarrow\rightarrow Mn^{IV}O_2 + HO_2^- \quad (7b)$$

Oxygen vacancy (OV) is a defect inside the manganese oxide crystalline materials, which can change the geometry and electronic structures and elongate the adsorbed oxygen O−O bond. Li et al. has studied the OV in β-MnO_2 along with the experiment and the density functional theory (DFT) calculation; their results concluded that moderate OV can lower the band gap, increase Fermi levels, and improve the ORR performance.[37] Similar results have been found in the literature.[8,38]

Therefore, α-MnO_2 has a better affinity to oxygen molecules and a higher activity toward ORR than that of β-MnO_2.[39] To the best of our knowledge, a thermal sensitivity and OV study in α-MnO_2 has not been reported yet. In this work, α-MnO_2 nanorods were synthesized by hydrothermal method and postheat treatment at various temperatures. The physical and electrochemical properties were studies on the original and thermal treated α-MnO_2 nanorods.

EXPERIMENTAL SECTION

α-MnO_2 Preparation. MnO_2 samples were synthesized by the hydrothermal method in an autoclave.[40] In brief, 0.2 g of $MnSO_4{\cdot}H_2O$ and 0.5 g of $KMnO_4$ (Sigma-Aldrich) were dissolved in 15 mL of DI water (Thermo Scientific Barnstead MicroPure, 18.2 MΩ.cm), transferred into the autoclave (PARR Instrument), and heated at 140 °C for 12 h. The precipitate was collected by centrifugation and washed thoroughly with DI water. The dark brown precipitate was dried at 80 °C and the sample was labeled as MO. The postheat treatments were carried out at 300, 400, and 500 °C in air for 2 h, and the samples were labeled MO300, MO400, and MO500, respectively.

Electrode Preparation and Testing. In order to increase the conductivity of the MnO_2 samples, 10 wt % of XC72 carbon was added before ink making. The CV and durability test was only conducted with manganese oxide film due to different stabilities of different carbon supports under oxidizing potential.[41] Typically, catalysts were dispersed in DI, 2-propanol. and Nafion dispersion (H_2O:2-propanol:Nafion (5 wt % Nafion, 1100 EW, Sigma-Aldrich) = 3:1:0.016 (V:V:V)) under ultrasonic treatment to form a 4 mg·mL^{-1} (Pt/C 1 mg·mL^{-1}) slurry. A thin catalyst film was deposited by dropping the required volume of the catalyst ink onto the polished glassy carbon disk (5 mm diameter, Pine Research AFE5T050GC). The loading of α-MnO_2 and Pt on working electrodes were ∼500 and ∼50 μg·cm^{-2}, respectively. The CVs in saturated N_2 and O_2 electrolytes used to show the redox profile, ∼ 125 μg·cm^{-2}, were

DOI: 10.1021/acs.inorgchem.9b00492
Inorg. Chem. XXXX, XXX, XXX−XXX

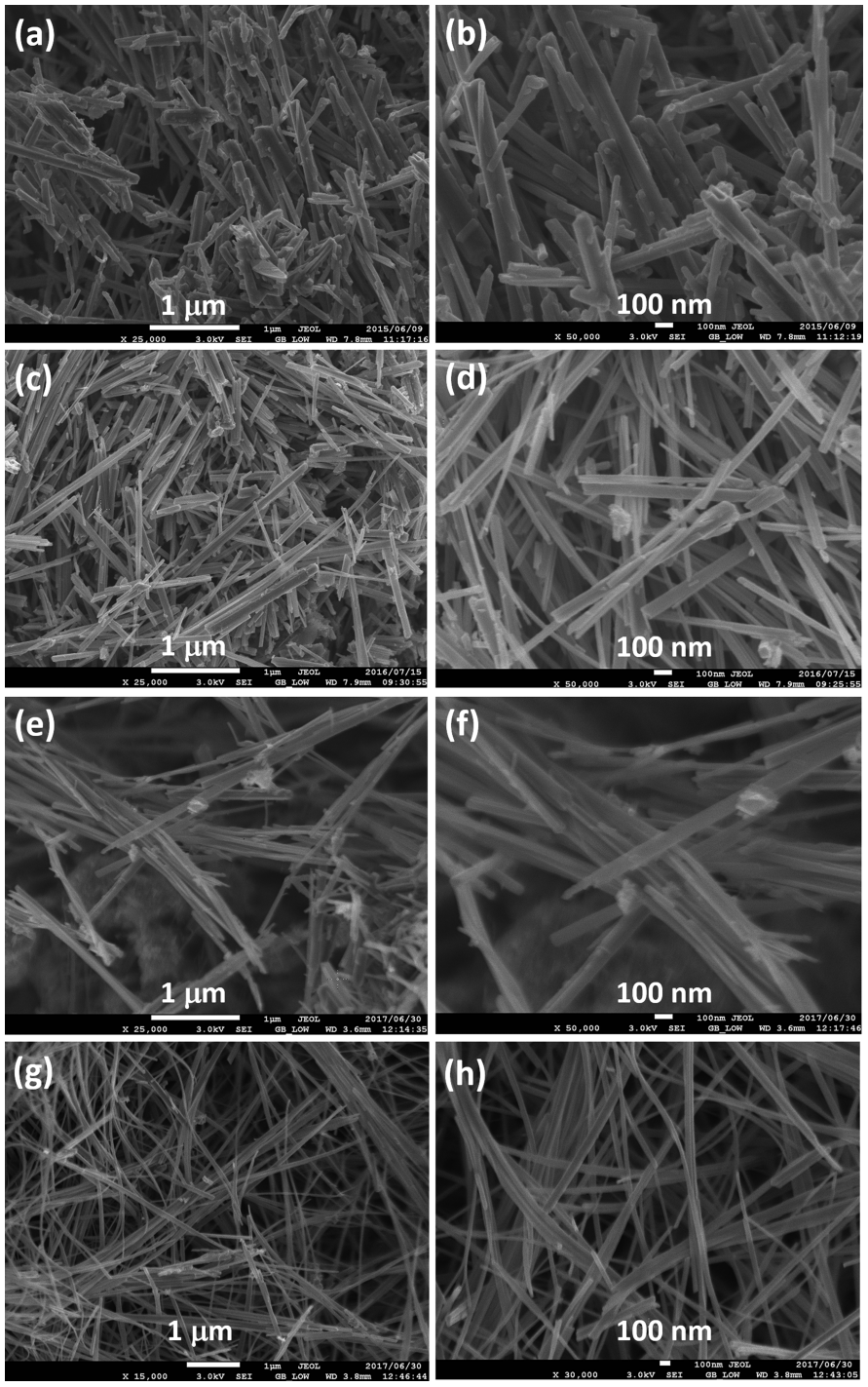

Figure 2. SEM of MO (a, b), MO300 (c, d), MO400 (e, f) and MO500 (g, h) at different magnifications.

employed on the working electrode. Uniform and well-adhered catalyst films were obtained by drying at ∼50 °C for 15 min under 700 rpm.

Linear sweep voltammetry (LSV) experiments were carried out in an O_2-saturated 1 M KOH solution, and all data were corrected by subtracting that with N_2-saturated solution. LSV experiments were conducted in the potential range of 1 to 0.2 vs RHE at 20 $mV{\cdot}s^{-1}$ scan rate with Pt rod as counter electrode and saturated calomel electrode as reference electrode using a PAR Bistat potentiostat at room temperature. In order to evaluate the stability of the catalyst, cyclic voltammetry (CV) was conducted for the disk electrodes at 50 $mV{\cdot}s^{-1}$ from 0.6 to 1.2 V vs RHE with a 500 rpm for 500 cycles in O_2-saturated 1 M KOH solution.[42] The chronoamperometries were tested at 0.8 V vs RHE for 14 h in O_2-saturated 1 M KOH solution at 400 rpm. The methanol tolerance tests were conducted in 1 M KOH with 1 M methanol content.

Materials Characterization. XRD analyses were recorded using Rigaku Ultima IV X-ray diffractometer with Cu Kα radiation (λ = 0.154 nm, 40 kV, and 30 mA). The morphology and structure of α-MnO_2 nanorods were evaluated by FESEM (JEOL-JSM 7500F at 2 and 3 keV). The high angle annular dark field (HAADF) images and electron energy loss spectroscopy (EELS) data was characterized by JEOL ARM-200F Scanning transmission electron microscopy (STEM) at 200 keV. XPS analysis were conducted in K-Alpha (Al, 12 kV, Thermo Scientific, East Grinstead, U.K.) with surface charging correction at 284.8 eV.

DOI: 10.1021/acs.inorgchem.9b00492
Inorg. Chem. XXXX, XXX, XXX−XXX

RESULTS AND DISCUSSION

The XRD patterns of the α-MnO_2 materials with/without heat treatment are given in Figure 1a. The sharp peaks were observed on all of samples at 2θ values of 12.75, 18.02, 28.79, and 37.45° correspond to (110), (200), (310), and (211) planes (PDF# 44-0142), respectively, indicating the high crystallinity of the α-MnO_2 samples. However, after 500 °C treatment, the α-Mn_2O_3 (PDF# 41-1442) peaks occur slightly at 23.13, 32.95 and 55.19° corresponding to (116), (222), and (440) planes, respectively, as α-MnO_2 is partially converted into α-Mn_2O_3. Under the same condition of XRD measurements, if a peak has higher integration intensity, it means that the crystal is preferred to form that specific plane.[43] To highlight the intensity of planes, Figure 1b summarized the peak area of planes on all the synthesized samples. For MO, MO300, and MO500 samples, the intensity of peaks decreases in the following order (310) > (200) > (211) > (110). For MO400 sample, the peak intensity drops as follows: (310) > (211) > (200) > (110). DFT calculation shows that (211) and (310) are the first and second most active planes toward ORR, respectively.[9] In this case, (211) was favorable growth on α-MnO_2 sample during 400 °C treatment.

In order to study the surface morphology of the synthesized materials, SEM was carried out and displayed in Figure 2. Parts a and b of Figure 2 show the α-MnO_2 nanorods shaped with an average ~80 nm diameter, ~1 μm length, and ~12.5 aspect ratio. Under 300 °C heating treatment, the surface of α-MnO_2 nanorods (Figure 2c,d) became smoother and thinner (~70 nm) in diameter and longer (~1.5 μm) in length with an aspect ratio of ~21.4. When the temperature was increased to 400 °C (Figure 2e,f), the MO400 nanorods tended to become sharper and longer, maintaining the same diameter as MO300 with an aspect ratio of ~28. When the temperature reached to 500 °C, MO500 materials stretched to nanowires. Even at lower magnifications, the wire ends are hard to observe (Figure 2g,h). In summary, as the temperature increases, the aspect ratios are increased, amd the MO nanorods tend to become thinner and longer.

EELS and HAADF were carried out by STEM for all four samples. Parts a–d of Figure 3 show the HAADF nanorod images for MO, MO300, MO400, and MO500, respectively. According to HAADF analysis, the darker the picture is, the lower atomic density will be. In this case, we can observe from HAADF images that the structure of α-MnO_2 nanorods were changed/collapsed with heating temperature. The untreated MO (Figure 3a) sample shows smooth and uniform atomic distributions with the least defects among all four samples. At 300 °C (Figure 3b), the appeared gray lines indicate the hollow channel was forming on α-MnO_2 nanorods during the heating. The darker lines were appeared on MO400 image (Figure 3c), indicating decreased atomic densities and hollow channels. In MO500 sample (Figure 3d), the HAADF image shows the nanorod was collapsed partly. It is evidence that the defects on α-MnO_2 nanorod were enhanced because of the form of Mn_2O_3 impurities from α-MnO_2 nanorods at 500 °C (seen in Figure 1).

In term of EELS analysis, dynamic scattering (scattered more than twice) will interfere the data interpretation. From published report,[44] the mean free path for a 200 keV energy electron in manganese oxide is ~100 nm. Based on the HAADF image, all the samples have great chance to be single scattered that indicate interference of dynamic scattering can be omitted. Figure 4 displays electron energy loss spectrum for OK and MnL2,3 edges on the prepared materials. The oxygen K edge starts at around 532 eV corresponding to the oxygen K shell core-loss, and the later signals start from 640 eV corresponding to the Mn $L_{2,3}$ core-loss (Figure 4a). The shape ranges from 50 eV after oxygen threshold, this will determine the Mn oxidation state, pointed out by Rask.[45] Since all four samples have relatively different O_K edges shapes (especially MO500), it can be seen from Figure 4a, the oxygen contents on MO300 and MO400 are slightly different from MO, and there is a huge difference observed on MO500 from the others. The magnified spectra of Mn loss on the samples were displayed in Figure 4b. The Mn edges consist of two major peaks: the first one starts at 640 eV, corresponding to the Mn L_3 core-loss, and the second one starts around 651 eV, attributed to Mn L_2. With increasing temperature, MnL_3 on α-MnO_2 materials was shifted to lower energy loss accordingly. The order of MnL_3 energy loss on samples is MO > MO300 > MO400 > MO500. The manganese valence is decreased (higher OV content) when the MnL_3 peaks shift to lower energy loss.[45−48] Therefore, the OV content in the manganese oxides decreases in the following order, MO400 > MO300 > MO, and MO400 achieved the highest OV content. Since the MO500 has a different phase proved by the XRD, it is difficult to compare it with other samples.

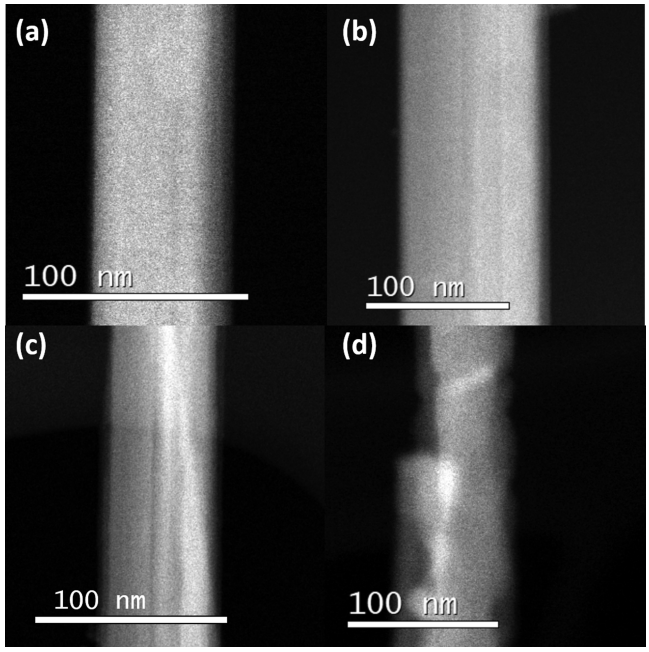

Figure 3. High angle annular dark field images of MO (a), MO300 (b), MO400 (c), and MO500 (d).

To analyze OV quantitates, the ratio of O and Mn intensity was calculated using Gatan DM software. In general, the hydrogenic model is accurate enough for K edges while the Hartree−Slater model is used for L edges.[49] The oxygen cross section is estimated based on the hydrogenic model and the manganese cross section estimation is based on the Hartree−Slater model. All the samples were calculated under same background and signal selecting condition using the above two models. And all the samples are based on a standard criterion with a stoichiometric formula of α-MnO_2. The results of quantitative analysis are listed in Table 1. It can be seen from Table 1 that the formulas of MO300, MO400, and MO500 are

DOI: 10.1021/acs.inorgchem.9b00492
Inorg. Chem. XXXX, XXX, XXX−XXX

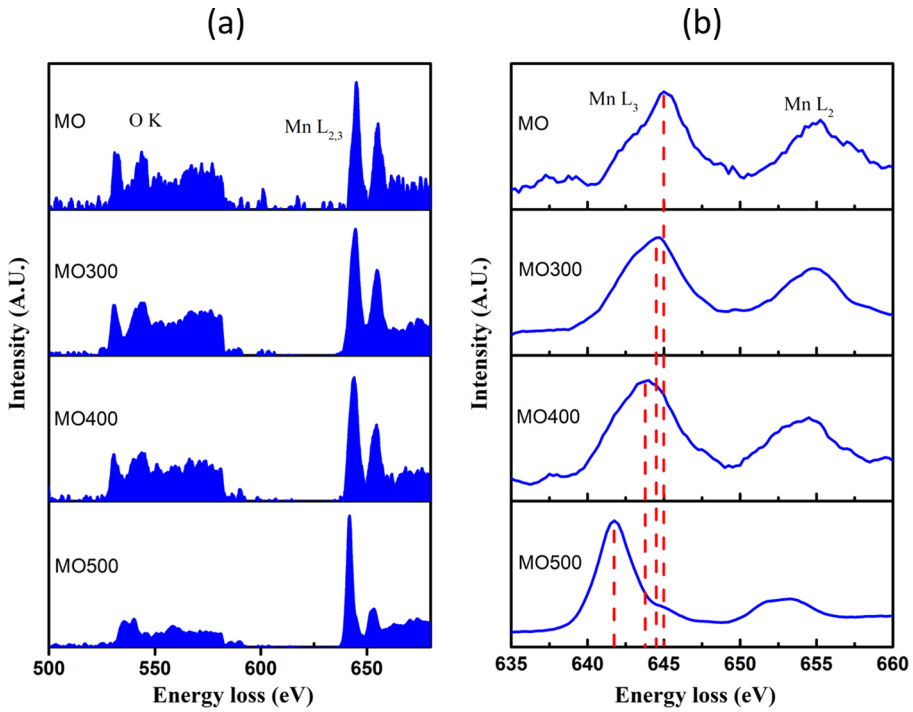

Figure 4. Electron energy loss spectrum (a) for O_K and $MnL_{2,3}$ edges of MO, MO300, MO400, and MO500, respectively, and (b) zoomed in $Mn_{L2,3}$ edges of MO, MO300, MO400, and MO500, respectively.

Table 1. List of Intensity Ratios of O/Mn and Mn $_{L3/L2}$ in All MnO_2 Samples

	MO	MO300	MO400	MO500
O:Mn ratio (Mn valence)	2.0 (+4)	1.86 (+3.72)	1.77 (+3.54)	1.10 (+2.2)
I(L3)/I(L2) (Mn valence)	1.79 (+4.05)	2.04 (+3.96)	2.12 (+3.9)	3.49 (+2.5)

$MnO_{1.86}$, $MnO_{1.77}$, and $MnO_{1.10}$, respectively. From the above results, the oxygen content trend decreases as the sintering temperature increased.

Another approach to determine Mn oxidation state is from the Mn intensity ratio of I(L3)/I(L2). From Table 1, the ratios of integrated intensity (area under the curve) on MO, MO300, MO400, and MO500 are 1.79, 2.04, 2.12 and 3.49, which by Kurata's method result in Mn formal valences of 4.05, 3.96, 3.9, and 2.5, respectively.[50] This analysis also gives evidence that, with increasing temperature, the Mn formal valence decreases therefore increasing OV. Oxygen vacancy is a defect inside the manganese oxides crystalline materials, the OV presence can change the geometry and electronics structures and elongate the O−O bond of the adsorbed oxygen. Moderate OV can improve the ORR performance found in β-MnO_2 and λ-MnO_2, if the OV content is too high, the material will change the structure and become a different phase.[8,38]

Figure 5 shows the deconvoluted peaks of the O 1s and Mn 2p spectra on MO, MO300, MO400 and MO500 materials. The three deconvolution peaks of O 1s (Figure 5a−d) are associated with Mn−O−Mn (529.79 eV) as lattice oxygen (O_{latt}), Mn−OH (531.26 eV), and H_2O adsorption (533.8 eV). The latter two are adsorption oxygen (O_{ad}).[51] From the quantification analysis, the ratios of O_{latt}/O_{ad} are 1.20, 1.08, 1.01, and 1.09 for MO, MO300, MO400, and MO500, respectively. The lower of the ratios indicates the stronger of the manganese oxides to adsorption; this could boost the ORR.[52] The high-resolution Mn 2p spectra of the prepared materials are shown in Figure 5e,f. Two peaks in the XPS spectra on all the samples are attributed to Mn $2p_{1/2}$ (654.04 eV) and Mn $2p_{3/2}$ (642.36 eV). The Mn 2p $_{3/2}$ peaks can be deconvoluted into four sub peaks P1 (640.80 eV), P2 (642.18 eV), P3 (643.54 eV), and P4 (645.08 eV). P1 is due to Mn^{3+} binding electrons, P2 and P3 are ascribed to Mn^{4+} ion and P4 belongs to shakeup satellite peak.[53] The integrated intensity of P1 is increasing with heating temperature, with value of 5.05, 5.54, 6.24, and 9.80% for MO, MO300, MO400, and MO500, respectively. From another viewpoint, the sum of P2 and P3 is decreasing with the increasing of the heating temperature at 87.04, 86.68, 86.12, and 79.67% for MO, MO300, MO400, and MO500, respectively. Those results indicated more Mn^{4+} is being reduced with temperature increased, which lead to less oxygen content inside the structure of the prepared materials. From the quantification of the XPS survey scan (see Figure 1S in SI), the chemical formula of MO, MO300, MO400, and MO500 can be assigned to MnO_2, $MnO_{1.98}$, $MnO_{1.91}$, and $MnO_{1.84}$, respectively. The oxygen content from XPS analysis is decreasing with increase heating temperature, which are corresponding with results of EELS. However, the XPS quantification showed higher oxygen content compared to the analysis of EELS, which caused from difference measurements from EELS and XPS, as EELS signal from the bulk and XPS signal from surface of the materials.

The CVs on MO, MO300, MO400, and MO500 electrodes in O_2- or N_2-saturated 1 M KOH are shown in Figure 6. The CVs in N_2 (Figure 6, black) on all the electrodes showed no observable redox peaks. However, in the O_2-saturated 1 M KOH, the CVs (Figure 6, red) showed a reduction current

DOI: 10.1021/acs.inorgchem.9b00492
Inorg. Chem. XXXX, XXX, XXX−XXX

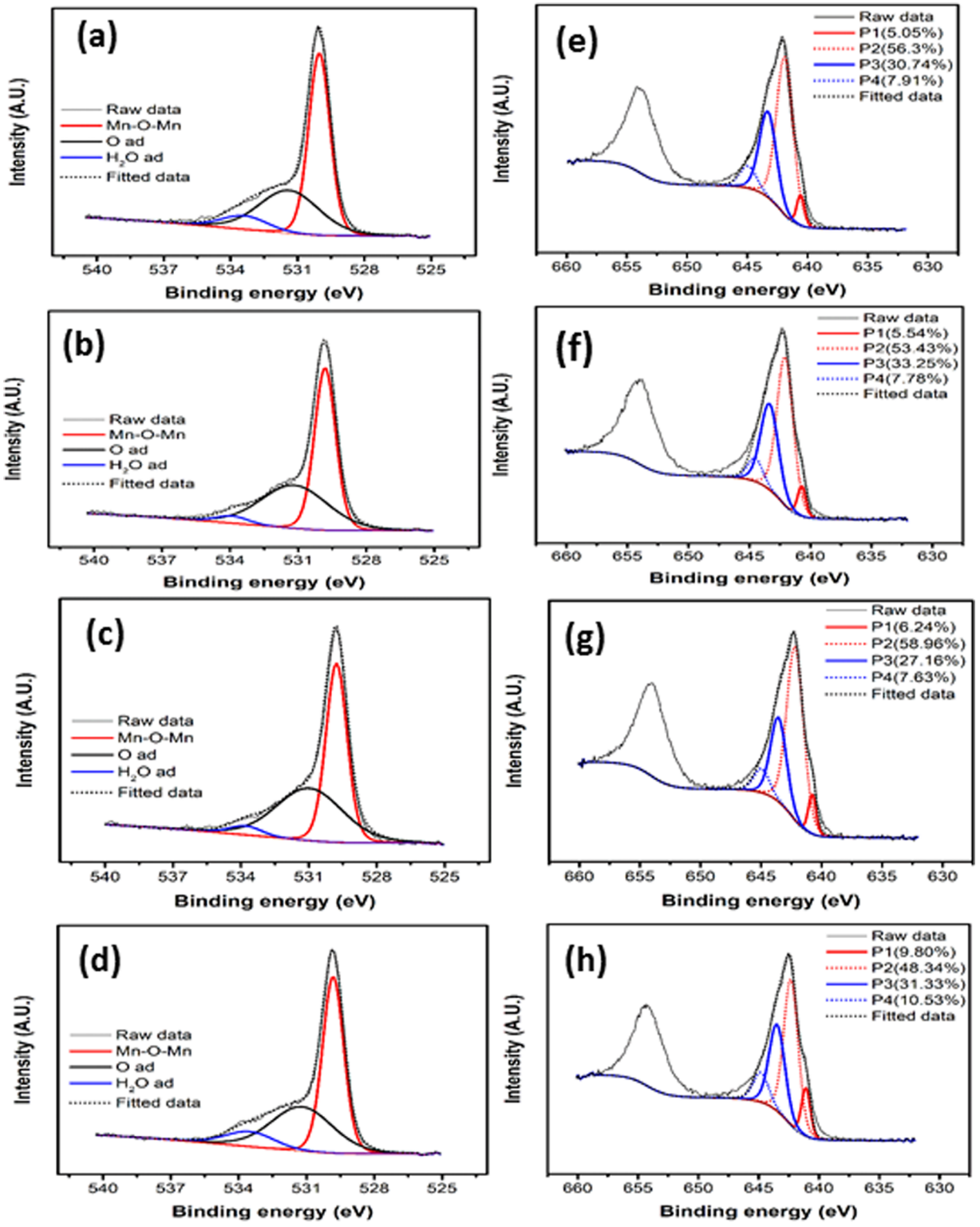

Figure 5. XPS spectra of O 1s in (a) MO, (b) MO300, and (c) MO400 and of Mn 2p in (e) MO, (f) MO300, (g) MO400, and (h) MO500.

which belongs to ORR. From the CV curves in O_2-saturated 1 M KOH, the visible two onset point is showing that there is a two-step reaction mechanism involved in all the samples. The first onset point could be attributed to eq 6b and eq 7b for a two-electron transfer process forming HO_2^-; when the greater reducing potential is introduced, the as formed HO_2^- is further being reduced to OH^-.[26] The second onset point of MO 400 starting at ~0.45 V vs RHE, is more positive than that for MO, MO300, and MO500 at 0.36, 0.37, and 0.34 V vs RHE, which indicates that MO 400 has better performance for ORR.

The electrochemical properties and durability performance on MnO_2 and Pt/C electrodes are shown in Figure 7. The LSV values on all the prepared samples and commercial Pt/C are shown in the Figure 7a. The half-wave potential and limiting current in Figure 7a are at 0.60, 0.62, 0.65, and 0.59 V vs RHE and −5.09, −5.52, −6.17, and −5.36 mA·cm^{-2} for MO,

DOI: 10.1021/acs.inorgchem.9b00492
Inorg. Chem. XXXX, XXX, XXX−XXX

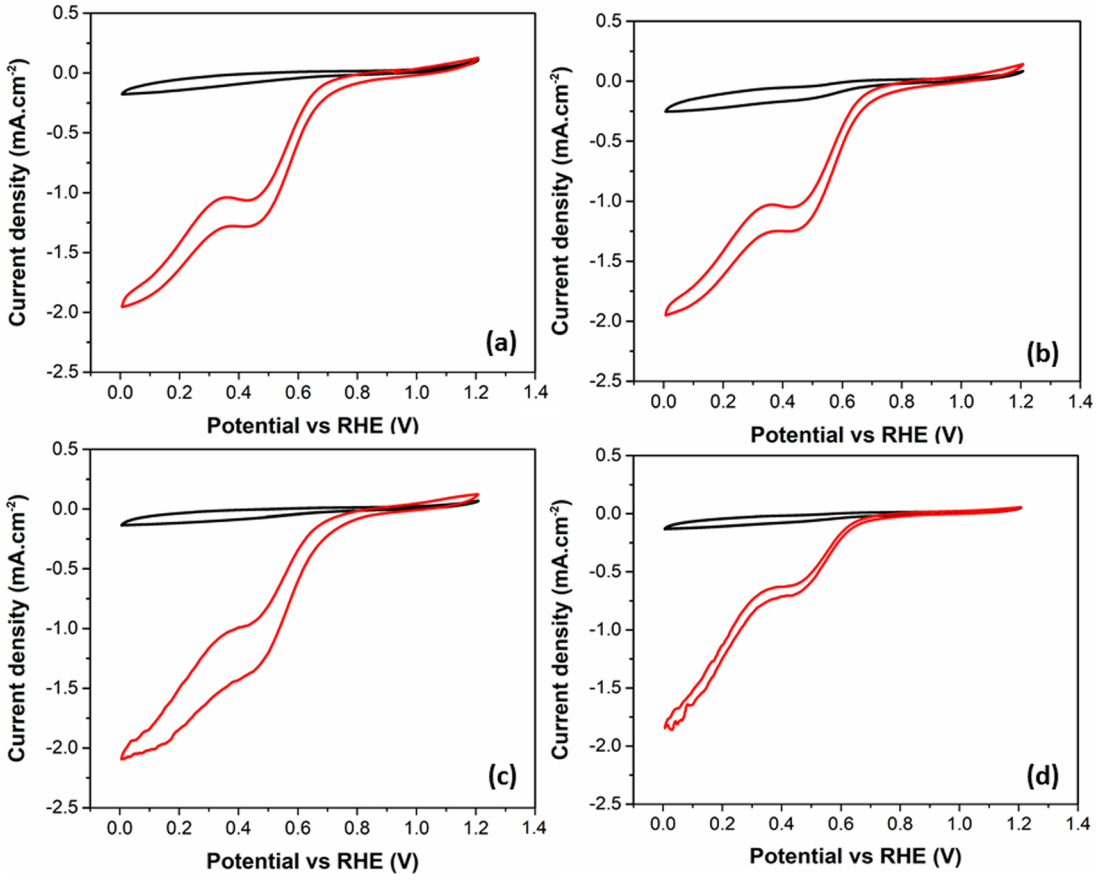

Figure 6. O_2 (red) and N_2 (black) CV in 1 M KOH electrolyte of (a) MO, (b) MO300, (c) MO400, and (d) MO500.

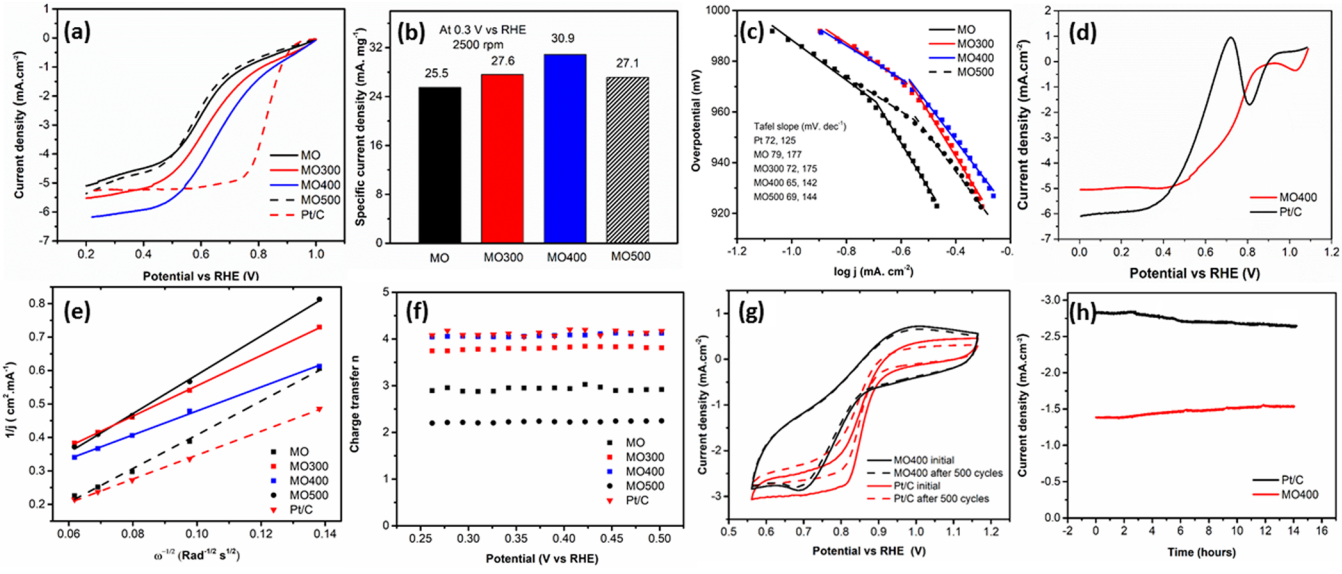

Figure 7. Electrochemical analysis of (a) LSV of MO (black), MO300 (red), MO400 (blue), MO500 (black-dash), and Pt/C (red-dash) with N_2 correction at 1600 rpm, (b) specific current density at 0.3 V vs RHE, MO (black), MO300 (red), MO400 (blue), and MO500 (black-white stripe), (c) Tafel slope of MO (black-solid), MO300 (red-solid), MO400 (blue-solid), MO500 (black-dash), and Pt/C (red-dash), (d) methanol tolerance in 1 M CH_3OH+1 M KOH on Pt/C (black) and MO400 (red), (e) the Koutecky–Levich (K-L) plot for MO (black-solid), MO300 (red-solid), MO400 (blue-solid), MO500 (black-dash), and Pt/C (red-dash), (f) the charge transfer number estimated from K-L analysis for MO (black-square), MO300 (red-square), MO400 (blue-square), MO500 (black-circle), and Pt/C (red-triangle), (g) CV data in O_2-saturated electrolyte at 500 rpm, MO400 (red) after 500 cycles (red-dash) and Pt/C (black) after 500 cycles (black-dash), and (h) chronoamperometry on Pt/C (black) and MO400 (red) for 14 h.

MO300, MO400, and MO500, respectively. With heating treatment up to 400 °C, both of the half-wave potential and limiting current were improved. The specific current densities (Figure 7b) of MO, MO300, MO400, and MO500 at 0.3 V vs

DOI: 10.1021/acs.inorgchem.9b00492
Inorg. Chem. XXXX, XXX, XXX−XXX

Table 2. List of Recent Published Manganese Oxide Catalyst Results toward ORR

sample	I_c (mA·cm^{-2}) at 1600 rpm	sweep rate (mV·s^{-1})	electrolyte	n
α-MnO_2 in CNT[57]	−3.6	5	1 M KOH	NA
α-MnO_2 out CNT[58]	−4.6	5	0.1 M KOH	NA
MN/NrGO[6]	−3.5	10	1 M KOH	3.83
MN/rGO[6]	−3.3	10	1 M KOH	3.34
MnO_2/rGO[59]	3.8	10	1 M KOH	3.85
MO/C	5.1	20	1 M KOH	2.90
MO300/C	5.52	20	1 M KOH	3.85
MO400/C	6.1	20	1 M KOH	4.00
MO500/C	5.3	20	1 M KOH	2.20

RHE are 25.5, 27.6, 30.9, and 27.1 mA·mg^{-1}, respectively. The specific current density increases with temperatures up to 400 °C and decreased at 500 °C. In addition, as displayed in Figure 7c, the Tafel slope of kinetic current of MO400 (65 mV·dec^{-1}) is the smallest among the samples, indicating the high ORR activity of MO400 at low overpotential,[54] and the value of the Tafel slope of MO400 close to $2.303RT/F$ (59 mV·dec^{-1} at 25 °C), in which reaction order on MO400 is similar to that of Mn_xO/C under O_2-saturated KOH solution[35] and γ-MnO_2 under air-saturated KOH solution is given.[55] In the kinetic and diffusion mixed control region, MO400 has the Tafel smallest slope at 142 mV·dec^{-1} as well. It is also an indicator of MO400 fast reaction kinetics toward ORR. From XRD, XPS, and EELS results, the MO400 has the highest (211) diffraction peak intensity and moderate OV content among all four samples, and these could be reasons for its best electrochemical performance. On the other hand, the species of Mn^{4+}/Mn^{3+} coexisted and was believed to favor the ORR on MnO_x/C,[35] and more Mn^{4+} on the surface of MnO_x have shown higher ORR activity than that with more Mn^{3+} species.[56] In this case, we believe the coexistence of Mn^{4+}/ Mn^{3+} species with certain ratios accelerates the charge transfer to oxygen and thus favors the oxygen reduction. The most favorable ratio of Mn^{4+}/Mn^{3+} was produced on MO400, which shows the best ORR activity.

The methanol tolerance tests were performed on MO400 and Pt/C electrodes in 1 M CH_3OH + 1 M KOH as shown in Figure 7d. The commerical Pt/C showed big methanol oxidation peaks at ∼0.7 V vs RHE. However, no peak of methanol oxidation was observed on the MO400 electrode. This indicates the MO400 material has a high methanol tolerance property compared to the commercial Pt/C catalyst.

The linear relationships of K-L analysis at 0.3 V vs RHE (Figure 7e) indicated the fast kinetics for all the materials. The calculated charge transfer number from K-L analysis on different potential was displayed in Figure 7f. The charger transfers number (n) of ORR on MO, MO300, MO400, MO500, and Pt was calculated as around 2.9, 3.8, 4, 2.2, and 4, respectively. The oxygen reduction on a Pt/C catalyst mainly proceed by a direct 4e$^-$ pathway (eq 1) with a serial 2 × 2 e$^-$ pathway,[26] which is in agreement with our result on commercial Pt/C. The oxygen reduction on MnO_x has been investigated to proceed to the first partial reaction with two electrons (eq 2) followed by either the 2e reduction (eq 3) or the chemical disproportionation (eq 4) of hydrogen peroxide (HO_2^-).[35] For the MO sample, n = 2.9 at E = 0.3 V vs RHE, showing that the ORR mechanism falls between 2- and 4-electron pathways. As a result, the HO_2^- yield is large. The ORR on MO300 is toward the 4-electron pathway (but not totally) as n is 3.8, indicating that the HO_2^- yield is small. The number of electrons (n) on MO400 is 4, showing that the ORR mechanism is 4-electron path and follows reaction routes of eq 5, eq 6a, and eq 7a. When the temperature reaches 500 °C, impurities of α-Mn_2O_3 formed. n is 2.2 on MO500, indicating the oxygen reduction toward the 2-electron path but with a small amount of HO_2^- yield. However, MO500 has the highest content of OV; when too much OV is introduced, the MnO_2 structure starts to collapse by forming Mn_2O_3, which changesthe electronic structure and adsorption energy, which is one possible reason to cause a 2-electron mechanism on MO500 catalyst.[37] The results demonstrated that thermal treatment on α-MnO_2 further directs the ORR toward the 4-electron path. Thus, the treatment on MnO_2 is of benefit to the kinetic of the ORR before 500 °C.

The stability comparison was carried out o MO400 and Pt/C by the CV technique and shown in the Figure 7g. After 500 cycles, the overpotential on Pt/C electrode increased by 12 mV at −1 mA.cm^{-2} and current density decreased by 9.5% from −3.07 to −2.77 mA.cm^{-2} at 0.6 V vs RHE on Pt/C electrode. However, the MO400 reduction current is increasing with cycles at the beginning, the MO400 is first cycled until the current is stable then test consecutive 500 cycles. After 500 cycles, overpotential on MO400 electrode increased by only 6 mV at −1 mA.cm^{-2} and current density decreased by 1.95% from −2.84 to −2.78 mA.cm^{-2} at 0.6 V vs RHE. The chronoamperometry was also performed for durability evaluation and shown as Figure 7h, for 14 h holding potential at 0.8 V vs RHE at 400 rpm with O_2 bubbling. The MO400 shows increasing the reduction current compare to the initial by 10%. In the meanwhile, the Pt/C decreased 5% reduction current after chronoamperometry testing. Evidently, the MO400 electrode shows higher stability compared to the commercial Pt/C electrocatalyst. Table.2 shows the LSV comparison with other manganese oxide catalysts in the literature. Our results on MnO_2 show slightly lower activity compared to the reported results. Because carbon was mixed with the prepared materials, which could cause less conductivity than those of MnO_2/C composites. However, with simple heat treatment on the α-MnO_2 materials, the ORR performances on the treated materials were boosted.

CONCLUSION

Pristine α-MnO_2 nanorods were synthesized. Thermal sensitivity of α-MnO_2 nanorods was studied under various calcination temperatures (300, 400, and 500 °C), and a series of α-MnOx with different Mn valences and OV content were generated from the pristine α-MnO_2 nanorods. With increasing temperature, the α-MnO_2 nanorods tend to become longer and thinner. At 500 °C, XRD showed the presence of Mn_2O_3 impurity in α-MnO_2. Quantification analysis of EELS spectrum and I(L3)/I(L2) methods have analyzed that the Mn state is

DOI: 10.1021/acs.inorgchem.9b00492
Inorg. Chem. XXXX, XXX, XXX−XXX

decreased with increasing temperature. The XPS also showed decreasing oxygen content with increasing heating temperature. The ORR onset potential and limiting/specific current were improved by increasing the temperature up to 400 °C, which then decreased due to too high of an OV content and Mn_2O_3 impurities on the MO500 sample. The methanol tolerance testing indicates the MO400 is highly ORR selective. In stability analysis, MO400 indicated higher durability after 500 cycles and 14 h chronoamperometry compared with commercial Pt/C. Overall, the catalytic activity of the α-MnOx toward ORR depends on the Mn valence state, OV content, and crystal structure.

■ ASSOCIATED CONTENT

Supporting Information

The Supporting Information is available free of charge on the ACS Publications website at DOI: 10.1021/acs.inorgchem.9b00492.

XPS survey spectra (PDF)

■ AUTHOR INFORMATION

Corresponding Author

*(H.Z.) E-mail: hzheng@csir.co.za.

ORCID

H. Zheng: 0000-0003-4180-0197

A. M. Kannan: 0000-0002-8412-1680

Notes

The authors declare no competing financial interest.

■ ACKNOWLEDGMENTS

The authors would like to thank CSIR, USAID (US-Pakistan Centers for Advanced Studies), and USAID (Global Development Research) for financial support. We acknowledge the use of facilities within the Eyring Materials Center at Arizona State University and XPS at LANNBIO Cinvestav Mérida, Mexico.

■ REFERENCES

(1) Tompsett, D. A.; Parker, S. C.; Bruce, P. G.; Islam, M. S. Nanostructuring of β-MnO_2: The Important role of surface to bulk ion migration. *Chem. Mater.* **2013**, *25*, 536−541.

(2) Minguzzi, A.; Longoni, G.; Cappelletti, G.; Pargoletti, E.; Di Bari, C. Di; Locatelli, C.; Marelli, M.; Rondinini, S.; Vertova, A. The Influence of carbonaceous catrices and electrocatalytic MnO_2 nanopowders on lithium-Air battery performances. *Nanomaterials* **2016**, *6*, 10.

(3) Hu, Y.; Zhang, T.; Cheng, F.; Zhao, Q.; Han, X.; Chen, J. Recycling application of Li − MnO_2 batteries as rechargeable lithium − Air batteries. *Angew. Chem., Int. Ed.* **2015**, *54*, 4338−4343.

(4) Pan, Z. F.; An, L.; Zhao, T. S.; Tang, Z. K. Advances and challenges in alkaline anion exchange membrane fuel cells. *Prog. Energy Combust. Sci.* **2018**, *66*, 141−175.

(5) Zhao, F.; Harnisch, F.; Schröder, U.; Scholz, F.; Bogdanoff, P.; Herrmann, I. Application of pyrolysed iron (II) phthalocyanine and CoTMPP based oxygen reduction catalysts as cathode materials in microbial fuel cells. *Electrochem. Commun.* **2005**, *7*, 1405−1410.

(6) Gautam, R. K.; Bhattacharjee, H.; Venkata Mohan, S.; Verma, A. Nitrogen doped graphene supported α-MnO_2 nanorods for efficient ORR in a microbial fuel cell. *RSC Adv.* **2016**, *6*, 110091−110101.

(7) Feng, Y.; Ye, F.; Liu, H.; Yang, J. Enhancing the methanol tolerance of platinum nanoparticles for the cathode reaction of direct methanol fuel cells through a geometric design. *Sci. Rep.* **2015**, *5*, 1−11.

(8) Lee, S.; Nam, G.; Sun, J.; Lee, J. S.; Lee, H. W.; Chen, W.; Cho, J.; Cui, Y. Enhanced Intrinsic catalytic activity of λ-MnO_2 by electrochemical tuning and oxygen Vacancy Generation. *Angew. Chem., Int. Ed.* **2016**, *55*, 8599−8604.

(9) Mainar, A. R.; Colmenares, L. C.; Leonet, O.; Alcaide, F.; Iruin, J. J.; Weinberger, S.; Hacker, V.; Iruin, E.; Urdanpilleta, I.; Blazquez, J. A. Manganese oxide catalysts for secondary zinc air batteries: from electrocatalytic activity to bifunctional air electrode performance. *Electrochim. Acta* **2016**, *217*, 80−91.

(10) Ma, H.; Wang, B.; Fan, Y.; Hong, W. Development and characterization of an electrically rechargeable zinc-air battery stack. *Energies* **2014**, *7*, 6549−6557.

(11) Li, G.; Mezaal, M. A.; Zhang, R.; Zhang, K.; Lei, L. Electrochemical performance of MnO_2 - based air cathodes for zinc-air batteries. *Fuel Cells* **2016**, *16*, 395−400.

(12) Post, J. E. Manganese oxide minerals : Crystal structures and economic and environmental significance. *Proc. Natl. Acad. Sci. U. S. A.* **1999**, *96*, 3447−3454.

(13) Pargoletti, E.; Cappelletti, G.; Minguzzi, A.; Rondinini, S.; Leoni, M.; et al. High-performance of bare and Ti-doped a -MnO_2 nanoparticles in catalyzing the Oxygen Reduction Reaction. *J. Power Sources* **2016**, *325*, 116−128.

(14) Lu, L.; Xu, H.; Shi, J.; Zhu, S.; Zhao, H.; Wang, G. Pt-supported C − MnO_2 as a catalyst for polymer electrolyte membrane fuel cells. *J. Appl. Electrochem.* **2018**, *48*, 801−810.

(15) Li, Y.; Cao, S.; Fan, L.; Han, J.; Wang, M.; Guo, R. Science hybrid shells of MnO_2 nanosheets encapsulated by N-doped carbon towards nonprecious oxygen reduction reaction catalysts. *J. Colloid Interface Sci.* **2018**, *527*, 241−250.

(16) Hang, Y.; Zhang, C.; Luo, X.; Xie, Y.; Xin, S.; Li, Y.; Zhang, D.; Goodenough, J. B. α -MnO_2 nanorods supported on porous graphitic carbon nitride as efficient electrocatalysts for lithium-air batteries. *J. Power Sources* **2018**, *392*, 15−22.

(17) Zhang, T.; Tham, N. N.; Liu, Z.; Fisher, A.; Lee, J. Y. Promotion of the bifunctional electrocatalytic oxygen activity of manganese oxides with dual-affinity phosphate. *Electrochim. Acta* **2018**, *277*, 143−150.

(18) Stoerzinger, K. A.; Risch, M.; Han, B.; Shao-horn, Y. Recent insights into manganese oxides in catalyzing oxygen reduction kinetics. *ACS Catal.* **2015**, *5*, 6021−6031.

(19) Song, C.; Zhang, J. Electrocatalytic Oxygen Reduction Reaction. *PEM fuel cell electrocatalyst and catalyst layers: Fundamentals and applications* **2008**, 89−134.

(20) Choi, C. H.; Kwon, H. C.; Yook, S.; Shin, H.; Kim, H.; Choi, M. Hydrogen peroxide synthesis via enhanced two-electron oxygen reduction pathway on carbon-coated Pt surface. *J. Phys. Chem. C* **2014**, *118*, 30063−30070.

(21) Liu, Y.; Sun, Q.; Li, W.; Adair, K. R.; Li, J.; Sun, X. A comprehensive review on recent progress in aluminum−air batteries. *Green Energy & Environ.* **2017**, *2*, 246−277.

(22) Liu, J.; Jiao, M.; Lu, L.; Barkholtz, H. M.; Li, Y.; Wang, Y.; Jiang, L.; Wu, Z.; Liu, D.; Zhuang, L.; et al. High performance platinum single atom electrocatalyst for oxygen reduction reaction. *Nat. Commun.* **2017**, *8*, 15938.

(23) Chatenet, M.; Aurousseau, M.; Durand, R.; Andolfatto, F. Silver-platinum bimetallic catalysts for oxygen cathodes in chlor-alkali electrolysis: Comparison with pure platinum. *J. Electrochem. Soc.* **2003**, *150*, D47−D55.

(24) Antoine, O.; Durand, R. RRDE study of oxygen reduction on Pt nanoparticles inside Nafion®: H_2O_2 production in PEMFC cathode conditions. *J. Appl. Electrochem.* **2000**, *30*, 839−844.

(25) Schneider, A.; Colmenares, L.; Seidel, Y. E.; Jusys, Z.; Wickman, B.; Kasemo, B.; Behm, R. J. Transport effects in the oxygen reduction reaction on nanostructured, planar glassy carbon supported Pt/GC model electrodes. *Phys. Chem. Chem. Phys.* **2008**, *10*, 1931−1943.

(26) Cheng, F.; Su, Y.; Liang, J.; Tao, Z.; Chen, J. MnO_2-based nanostructures as catalysts for electrochemical oxygen reduction in alkaline media. *Chem. Mater.* **2010**, *22*, 898−905.

(27) Mao, L.; Zhang, D.; Sotomura, T.; Nakatsu, K.; Koshiba, N.; Ohsaka, T. Mechanistic study of the reduction of oxygen in air

DOI: 10.1021/acs.inorgchem.9b00492
Inorg. Chem. XXXX, XXX, XXX−XXX

electrode with manganese oxides as electrocatalysts. *Electrochim. Acta* **2003**, *48*, 1015−1021.
(28) Mao, L.; Sotomura, T.; Nakatsu, K.; Koshiba, N.; Zhang, D.; Ohsaka, T. Electrochemical characterization of catalytic activities of manganese oxides to oxygen reduction in alkaline aqueous solution. *J. Electrochem. Soc.* **2002**, *149*, A504−A507.
(29) El-Deab, M. S.; Ohsaka, T. Manganese oxide nanoparticles electrodeposited on platinum are superior to platinum for oxygen reduction. *Angew. Chem., Int. Ed.* **2006**, *45*, 5963−5966.
(30) Lima, F. H. B.; Calegaro, M. L.; Ticianelli, E. A. Investigations of the catalytic properties of manganese oxides for the oxygen reduction reaction in alkaline media. *J. Electroanal. Chem.* **2006**, *590*, 152−160.
(31) Lima, F. H. B.; Calegaro, M. L.; Ticianelli, E. A. Electrocatalytic activity of manganese oxides prepared by thermal decomposition for oxygen reduction. *Electrochim. Acta* **2007**, *52*, 3732−3738.
(32) Gong, K.; Yu, P.; Su, L.; Xiong, S.; Mao, L. Polymer-assisted synthesis of manganese dioxide/carbon nanotube nanocomposite with excellent electrocatalytic activity toward reduction of oxygen. *J. Phys. Chem. C* **2007**, *111*, 1882−1887.
(33) Verma, A.; Jha, A. K.; Basu, S. Manganese dioxide as a cathode catalyst for a direct alcohol or sodium borohydride fuel cell with a flowing alkaline electrolyte. *J. Power Sources* **2005**, *141*, 30−34.
(34) Ohsaka, T.; Mao, L.; Arihara, K.; Sotomura, T. Bifunctional catalytic activity of manganese oxide toward O_2 reduction: novel insight into the mechanism of alkaline air electrode. *Electrochem. Commun.* **2004**, *6*, 273−277.
(35) Roche, I.; Chaînet, E.; Chatenet, M.; Vondrák, J. Carbon-supported manganese oxide nanoparticles as electrocatalysts for the oxygen reduction reaction (ORR) in alkaline medium: physical characterizations and ORR mechanism. *J. Phys. Chem. C* **2007**, *111*, 1434−1443.
(36) Cao, Y. L.; Yang, H. X.; Ai, X. P.; Xiao, L. F. The mechanism of oxygen reduction on MnO_2 -catalyzed air cathode in alkaline solution. *J. Electroanal. Chem.* **2003**, *557*, 127−134.
(37) Li, L.; Feng, X.; Nie, Y.; Chen, S.; Shi, F.; Xiong, K.; Ding, W.; Qi, X.; Hu, J.; Wei, Z.; Wan, L.-J.; Xia, M. Insight into the effect of oxygen vacancy concentration on the catalytic performance of MnO_2. *ACS Catal.* **2015**, *5*, 4825−4832.
(38) Ma, Y.; Wang, R.; Wang, H.; Key, J.; Ji, S. Control of MnO_2 nanocrystal shape from tremella to nanobelt for ehancement of the oxygen reduction reaction activity. *J. Power Sources* **2015**, *280*, 526−532.
(39) Zheng, H.; Modibedi, M.; Mathe, M.; Ozoemena, K. The thermal effect on the catalytic activity of MnO_2 (α, β, and γ) for oxygen reduction reaction. *Mater. Today Proc.* **2017**, *4*, 11624−11629.
(40) Cheng, F.; Zhao, J.; Song, W.; Li, C.; Ma, H.; Chen, J.; Shen, P. Facile controlled synthesis of MnO_2 nanostructures of novel shapes and their application in batteries. *Inorg. Chem.* **2006**, *45*, 2038−2044.
(41) Shinozaki, K.; Zack, J. W.; Richards, R. M.; Pivovar, B. S.; Kocha, S. S. Oxygen reduction reaction measurements on platinum electrocatalysts utilizing rotating disk electrode technique. *J. Electrochem. Soc.* **2015**, *162*, F1144−F1158.
(42) Shi, X.; Iqbal, N.; Kunwar, S. S.; Wahab, G.; Kasat, H. A.; Kannan, A. M. Pt Co@NCNTs cathode catalyst using ZIF-67 for proton exchange membrane fuel cell. *Int. J. Hydrogen Energy* **2018**, *43*, 3520.
(43) Cullity, B. D.; Stock, S. R. *Elements of X-ray Diffraction*, 1st ed.; Cohen, M., Ed.; Addison-Wesley: Reading, MA, 1956.
(44) Iakoubovskii, K.; Mitsuishi, K.; Nakayama, Y.; Furuya, K. Mean free path of inelastic electron scattering in elemental solids and oxides using transmission electron microscopy: Atomic number dependent oscillatory behavior. *Phys. Rev. B: Condens. Matter Mater. Phys.* **2008**, *77*, 104102.
(45) Rask, J. H.; Miner, B. A.; Buseck, P. R. Determination of manganese oxidation states in solids by electron energy-loss spectroscopy. *Ultramicroscopy* **1987**, *21*, 321−326.
(46) Cramer, S. P.; Ma, Y.; Chen, C. T.; Sette, F.; Libby, E.; Christou, G.; deGroot, F. M. F.; Fuggle, J. C.; Mullins, O. C.; Kipke, C. A.; Eichhorn, D. M.; Chan, M. K.; Armstrong, W. H.; Brooker, S.; McKee, V.; et al. Ligand field strengths and oxidation states from manganese L-edge spectroscopy. *J. Am. Chem. Soc.* **1991**, *113*, 7937−7940.
(47) Paterson, J. H.; Krivanek, O. L. Elnes of 3d transition-metal oxides. *Ultramicroscopy* **1990**, *32*, 319−325.
(48) Cotton, F. A. Metal-Metal Multiple Bonds and Metal Clusters. *In reactivity of metal−metal bonds: ACS Symp. Ser.* **1981**, *155*, 1−16.
(49) Olszta, M. J.; Wang, J.; Dickey, E. C. Stoichiometry and valence measurements of niobium oxides using electron energy-loss spectroscopy. *J. Microsc.* **2006**, *224*, 233−241.
(50) Kurata, H.; Colliex, C. Electron-energy-loss core-edge structures in manganese oxides. *Phys. Rev. B: Condens. Matter Mater. Phys.* **1993**, *48*, 2102−2108.
(51) Zhang, T.; Cheng, F.; Du, J.; Hu, Y.; Chen, J. Efficiently enhancing oxygen reduction electrocatalytic activity of MnO_2 using facile hydrogenation. *Adv. Energy Mater.* **2015**, *5*, 1400654.
(52) Cheng, G.; Xie, S.; Lan, B.; Zheng, X.; Ye, F.; Sun, M.; Lu, X.; Yu, L. Phase controllable synthesis of three-dimensional star-like MnO_2 hierarchical architectures as highly efficient and stable oxygen reduction. *J. Mater. Chem. A* **2016**, *4*, 16462−16468.
(53) Biesinger, M. C.; Payne, B. P.; Grosvenor, A. P.; Lau, L. W. M.; Gerson, A. R.; Smart, R. S. C. Resolving surface chemical states in XPS analysis of first row transition metals, oxides and hydroxides: Cr, Mn, Fe, Co and Ni. *Appl. Surf. Sci.* **2011**, *257*, 2717−2730.
(54) Zhang, Y.; Wang, X.; Hu, D.; Xue, C.; Wang, W.; Yang, H.; Li, D.; Wu, T. Monodisperse ultrasmall manganese-doped multimetallic oxysulfide nanoparticles as highly efficient oxygen reduction electrocatalyst. *ACS Appl. Mater. Interfaces* **2018**, *10*, 13413−13424.
(55) Cao, Y. L.; Yang, H. X.; Ai, X. P.; Xiao, L. F. The mechanism of oxygen reduction on MnO_2-catalyzed air cathode in alkaline solution. *J. Electroanal. Chem.* **2003**, *557*, 127−134.
(56) Hasan, M. A.; Zaki, M. I.; Pasupulety, L.; Kumari, K. Promotion of the hydrogen peroxide decomposition activity of manganese oxide catalysts. *Appl. Catal., A* **1999**, *181*, 171−179.
(57) Chen, G.; Sunarso, J.; Zhu, Y.; Yu, J.; Zhong, Y.; Zhou, W.; Shao, Z. Highly active carbon/α-MnO_2 hybrid oxygen reduction reaction Electrocatalysts. *ChemElectroChem* **2016**, *3*, 1760−1767.
(58) Guo, D.; Dou, S.; Li, X.; Xu, J.; Wang, S.; et al. Hierarchical MnO_2/rGO hybrid nanosheets as an efficient electrocatalyst for the oxygen reduction reaction. *Int. J. Hydrogen Energy* **2016**, *41*, 5260−5268.

DOI: 10.1021/acs.inorgchem.9b00492
Inorg. Chem. XXXX, XXX, XXX−XXX